Applied Materials Today 000 (2020) 100718

Contents lists available at ScienceDirect

Applied Materials Today

journal homepage: www.elsevier.com/locate/apmt

Wafer-scale 2D $PtTe_2$ layers-enabled Kirigami heaters with superior mechanical stretchability and electro-thermal responsiveness

Tae-Jun Ko[a], Sang Sub Han[a,b], Emmanuel Okogbue[a,c], Mashiyat Sumaiya Shawkat[a,c], Mengjing Wang[a], Jinwoo Ma[b], Tae-Sung Bae[d], Shihab Bin Hafiz[e], Dong-Kyun Ko[e], Hee-Suk Chung[d], Kyu Hwan Oh[b], Yeonwoong Jung[a,c,f,*]

[a] NanoScience Technology Center, University of Central Florida, Orlando, Florida 32826, USA
[b] Department of Materials Science and Engineering, Seoul National University, Seoul 08826, Republic of Korea
[c] Department of Electrical and Computer Engineering, University of Central Florida, Orlando, Florida 32816, USA
[d] Analytical Research Division, Korea Basic Science Institute, Jeonju 54907, Republic of Korea
[e] Department of Electrical and Computer Engineering, New Jersey Institute of Technology, Newark, New Jersey 07102, USA
[f] Materials Science and Engineering, University of Central Florida, Orlando, Florida 32816, USA

ARTICLE INFO

Article history:
Received 26 March 2020
Revised 28 May 2020
Accepted 29 May 2020
Available online xxx

Keywords:
Transition metal dichalcogenide
2D $PtTe_2$
Stretchable electronics
Wearable heater
Kirigami

ABSTRACT

With increasing interests in emergent wearable technologies such as e-skin healthcare devices, it is essential to develop new materials that can satisfy their demanded attributes; e.g., mechanical strain-invariant electrical and thermal properties. In this regard, two-dimensional (2D) transition metal dichalcogenide (TMD) layered materials have received tremendous attention owing to their intrinsic suitability, such as large tolerance limits under mechanical deformation coupled with decent electrical and thermal properties. However, these intrinsic advantages are often compromised upon their large wafer-scale integrations onto deformable substrates, which is commonly observed with conventional liquid-based or mechanical exfoliation approaches. In this paper, we demonstrate high-performance electrically-stretchable heaters by combining 2D platinum ditelluride ($PtTe_2$) layers – a relatively unexplored class of 2D TMDs – with a strain engineering design scheme. We directly grew wafer-scale 2D $PtTe_2$ layers on soft polyimide (PI) substrates by taking advantage of their low growth temperature. We verified their intrinsically low sheet resistance as low as 19.4 Ω/□ (thus, high electrical conductivity), which is superior to most other 2D TMDs. We then explored their Joule heating efficiencies and demonstrated they greatly surpass the performances of previously explored flexible heaters employing state-of-the-art nanomaterials including graphene, silver nanowires (Ag NWs), carbon nanotubes (CNTs) and their hybrids. By employing Kirigami patterning approaches for judicious strain engineering, we developed high-efficiency skin attachable 2D $PtTe_2$ layers-based Kirigami heaters, which exhibited nearly strain-invariant excellent electrical-thermal properties; e.g., voltage-driven reliable heat generation upon a cyclic application/termination of 70% tensile stretch for 1000 times. We believe this study on intrinsically metallic 2D layered material will open up new venues for futuristic high-performance large-scale stretchable electronic applications of wearable thermotherapy, e-textile, and soft actuators.

1. Introduction

Two-dimensional (2D) van der Waals (vdW) crystals employing transition metal dichalcogenides (TMDs) have inspired numerous innovations in a wide range of electrical applications previously foreseen to be impossible. Substantial efforts have been driven to explore refractory metals (e.g., molybdenum (Mo) or tungsten (W))-based semiconducting 2D TMD layers pursuing applications in digital electronics. Recently, metallic or semi-metallic 2D TMD layers are gaining increasing interests projecting unprecedented opportunities beyond them. These materials are in the form

Abbreviations: (vdW), Van der Waals; (TMDs), Transition metal dichalcogenides; ($PtTe_2$), 2D platinum ditelluride; (CNTs), Carbon nanotubes; (Ag NWs), Silver nanowires; (CVD), Chemical vapor deposition; (PI), Polyimide; (AFM), Atomic force microscopy; (TEM), Transmission electron microscopy; (IR), Infrared; (FEM), Finite element method; (EDS), Energy-dispersive X-ray spectroscopy; (STEM), Scanning transmission electron microscope; (SAED), Selected area electron diffraction; (XPS), X-ray photoelectron spectroscopy; (FFT), Fast Fourier transform.

* Corresponding author at: University of Central Florida, United States
E-mail address: Yeonwoong.Jung@ucf.edu (Y. Jung).

https://doi.org/10.1016/j.apmt.2020.100718
2352-9407/

of MX_2, where M represents noble metals in place of Mo or W, and X represents chalcogen elements. For instance, platinum (Pt)-based 2D TMDs\layers, i.e., 2D PtX_2, exhibit a large number of unusual yet attractive properties such as intrinsic electron-magnetic responsiveness and low synthesis temperature absent in conventional semiconducting 2D TMDs [1-4]. Particularly, 2D Pt ditelluride ($PtTe_2$) layers are an emerging class of metallic vdW crystals possessing unusual band structure and topological transition as well as extremely high electrical conductivity, i.e., ~10^6 - 10^7 S/m [5-7]. Moreover, they exhibit high air- and thermal-stability, unlike the black phosphorus of comparable electrical conductivity, which suffers from significant oxidation-driven properties degradation [8,9]. These combined attributes of high electrical conductivity and superior air/thermal stability coupled with their extremely small thickness project unprecedented opportunities that is difficult to achieve with any conventional 2D TMD layers or other metallic materials. Out of vastly projected applications, we particularly note their potential as an atomically thin "electrothermal material" which converts electric current into thermal energy. For decades, a large number of metallic materials with high electric-to-thermal conversion rates have been explored for a variety of electrothermal applications such as window defrosters/defoggers [10,11], thermotherapy pads [12,13], heating textiles [14], soft actuator [15], and smart drug delivery [16]. Recent advances in emerging technologies of various form factors, e.g., stretchable or foldable heaters, have demanded "ultra-light" electrothermal materials in mechanically adaptable forms. A variety of low-dimensional materials have been explored to overcome the intrinsic limitations (e.g., rigidity and bulkiness) of conventional electrothermal materials [17]. Earlier efforts have focused on combining one-dimensional (1D) conductive nanomaterials such as carbon nanotubes (CNTs) or silver nanowires (Ag NWs) with elastic and conjugated polymers [18-21] benefiting from their process simplicity. However, several drawbacks are noted in this approach; (1) It is difficult to achieve the high spatial homogeneity of electrothermal conversions on large areas as they occur by the percolation-driven transport of electrons/phonons owing to the intrinsic randomness of the way that the 1D nanomaterials are integrated. (2) Resulting composites are prone to thermally-driven mechanical deformation owing to the thermal instability of polymer constituents combined with their uneven interfaces with the 1D nanomaterials. Accordingly, significant performance degradations are noted upon repeated heating [22,23]. (3) It is challenging to reduce their thickness and maintain the high conductivity of 1D component-based composites at the same time, while the recent advances in wearable technologies have been driven toward incorporating thinner and more flexible/stretchable materials [17].

Recently, standalone inorganic 2D materials such as graphene or MXenes have been explored for mechanically deformable electrothermal heaters owing to their intrinsically superior electrical conductivity and mechanical adaptability [10,13,24-27]. However, several major drawbacks are noted in these approaches. For graphene, its very high growth temperature (e.g., > 900 °C for growth on copper substrates [10,24,25]) inevitably requires additional steps for transferring and integrating it on secondary target substrates, often causing unstable interfacial adhesion to the substrates [10]. Also, the crystallinity of MXenes integrated by conventional solution-based integration methods can significantly degrade with repeated humidity exposure, which requires additional protection layers leading to weight increment [27]. Accordingly, these approaches incongruently fail to achieve the originally projected advantages of ultra-low weight with high electric-to-thermal conversion rates accompanying high structural adaptability.

In this study, we explore electrothermal properties of chemically-grown 2D $PtTe_2$ layers and demonstrate their application for high-performance extremely stretchable wearable heaters. We grew wafer-scale 2D $PtTe_2$ multilayers via a chemical vapor deposition (CVD)- tellurization of Pt thin films at a low temperature of 400 °C, which is compatible with some polymeric substrates. We characterized their electrical properties and identified intrinsically small sheet resistance down to 19.4 Ω/□, significantly smaller than those of previously developed any other 2D materials. By taking this combined advantage of low growth temperature and high electrical conductance, we developed 2D $PtTe_2$ layers-based stretchable and wearable heaters by directly growing them on strain-engineered polymeric substrates of Kirigami forms and evaluated their electrothermal performances. These 2D $PtTe_2$ layers-based heaters exhibited remarkably fast electric-to-thermal conversion rates even at low applied voltages (i.e., 26.6 °C/sec of the heating rate at 5 V). Moreover, these superior properties were identified to be strain-invariant with extremely high mechanical tolerance, benefiting from the judiciously-designed Kirigami patterns– i.e., persistent heat generation even after 1,000 times cyclic stretching. Overall, the electrothermal performances of these CVD-grown wafer-scale 2D $PtTe_2$ layers greatly surpass those of all other state-of-the-art 1D or 2D materials previously explored for such applications, including Ag NWs, graphene, and MXenes.

2. Material and methods

2.1. 2D $PtTe_2$ synthesis

Pt seed films of controlled thickness from 0.5 to 9 nm were deposited on two kinds of substrates, i.e., silicon dioxide (SiO_2)/Si wafers (300 nm oxide layer thickness) and polyimide (PI) sheets (50 mm thickness) by an electron beam evaporator (Thermionics VE-100) at a deposition rate of 0.15 Å/sec. The Pt-deposited substrates were placed at the center of the quartz tube inside a CVD thermal furnace (Blue M Mini-Mite, Lindberg). Tellurium (Te) powder (CAS No. 13494-80-9, 200 mesh, 99.8%, Sigma-Aldrich, Inc.) contained in an alumina boat was placed at the upstream side of the furnace. The quartz tube containing the samples was evacuated to a basal pressure of < 20 mTorr, and argon (Ar) gas was subsequently supplied at a rate of 100 sccm to maintain the working pressure of 75 mTorr. Then, the furnace was heated up to 400 °C in 50 min, and the temperature was maintained for an additional 50 min before its natural cool-down to ambient temperature. After sample preparation, the thicknesses of 2D $PtTe_2$ layers were measured using atomic force microscopy (AFM, NanoIR2, Anasys Instruments) with tapping mode at 0.3 Hz of the scan rate.

2.2. Crystal structure characterization

Aberration-corrected transmission electron microscopy (Cs-corrected TEM, ARM 200F, Jeol, USA) was utilized with 200 kV of an accelerating voltage. For the plane-view TEM observation, as-grown 2D $PtTe_2$ layers were detached from SiO_2/Si wafers by using a buffered oxide etchant, and they were subsequently transferred onto copper TEM grids. For the cross-sectional TEM observation, standard focused ion beam lift-out techniques were employed for sample preparation. Also, X-ray diffraction (XRD, PANalytical Empyrean) was carried out for revealing the crystal structure of 2D $PtTe_2$ layers on SiO_2/Si substrates with a copper X-ray source ($K\alpha_1$, λ=1.5406 Å).

2.3. Raman and electrical characterization

Raman spectra of 2D $PtTe_2$ layers were acquired by inVia™ confocal Raman microscope (Renishaw, UK) at ambient condition. A laser source with 532 nm of wavelength was used for analysis, and the excitation power was set to 1 mW to minimize damage on the samples. The electrical properties of 2D $PtTe_2$ layers were

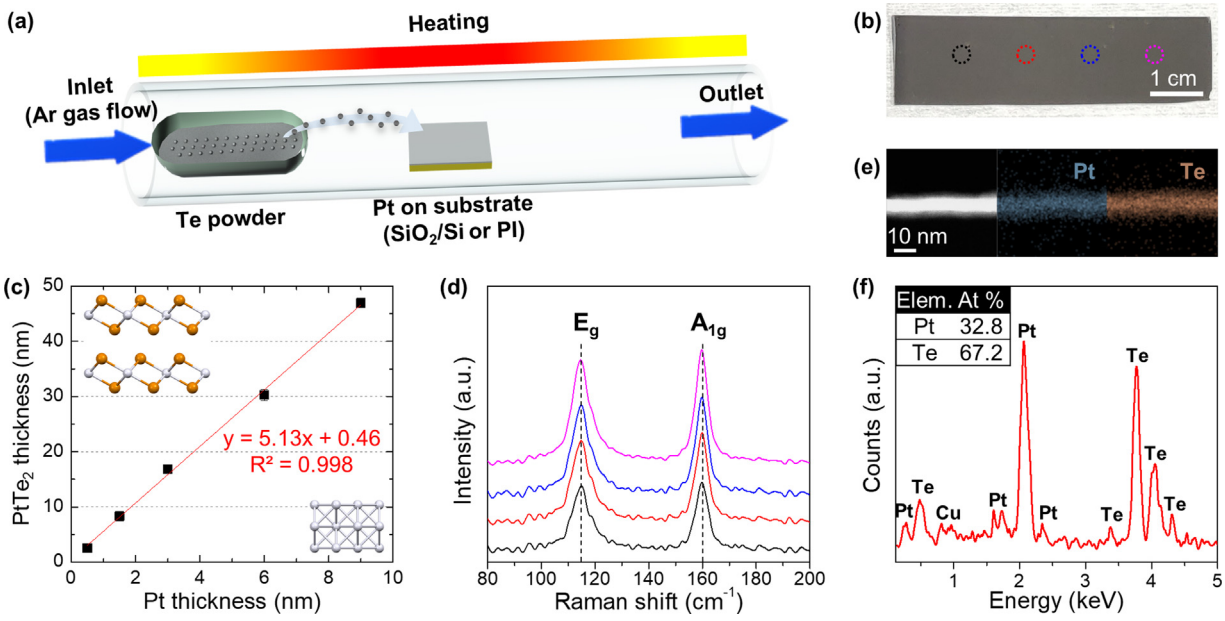

Fig. 1. (a) Schematic of CVD growth of wafer-scale 2D $PtTe_2$ layers. (b) A photo of 2D $PtTe_2$ layers grown on a SiO_2/Si wafer on a size of 12 cm^2. (c) Thickness relation of initial Pt films vs. resulting 2D $PtTe_2$ layers. (d) Raman spectra corresponding to the four spots marked on the sample in (b). (e) Cross-sectional TEM/EDS mapping images showing the spatial distribution of Pt and Te within 2D $PtTe_2$ layers. (f) EDS profile quantifying the atomic ratio of Pt and Te corresponding to (e).

characterized by current-voltage (I-V) measurements using a semiconductor parameter analyzer (HP 4156 A, Hewlett-Packard, USA) connected to a home-built probe station. Sheet resistances of 2D $PtTe_2$ layers were obtained by a 4-point resistivity probe (SP4, Signatone, USA) connect to a source meter (Keithley 2400, Keithley Instruments, USA).

2.4. Heating performance test

Joule heating performances of 2D $PtTe_2$ layers were evaluated by measuring their temperature change under an application of electrical bias. 2D $PtSe_2$ layers grown PI substrates with a size of 1.5 × 1.5 cm^2 were prepared, followed by the deposition of gold (Au) electrodes (100 nm thickness), achieving the active heating zone of 1 × 1.5 cm^2 in a two-terminal configuration. A power supply (TP3005T Variable Linear DC Power Supply, Tekpower, USA) was used to apply DC voltage to the samples in the range of 1 to 10 V. The maximum temperature profiles of the electrically-biased samples were recorded by an infrared (IR) camera (FLIR C2, FLIR® Systems, Inc., USA) with 9 Hz, and the heating and cooling rates were calculated from the temperature profile per second.

2.5. Kirigami-pattern fabrication and finite element method

Kirigami patterns were engraved on PI substrates by a commercial mechanical cutter (Cricut Explore Air 2, Cricut, Inc., USA). Then, 2D $PtTe_2$ layers were grown on the patterned substrates by the CVD tellurization method, as described above. Deformation behaviors of the Kirigami patterns were analyzed by the finite element method (FEM) simulation using commercial software (Abaqus 6.13). S4R type element with an approximate mesh size of 50 mm was used.

3. Results and Discussion

3.1. 2D $PtTe_2$ layer growth

2D $PtTe_2$ layers were grown by the CVD tellurization of Pt-deposited growth substrates following the growth recipe presented in the Material and methods section (Fig. 1a). Briefly, Pt-deposited substrates are placed in the furnace center zone and vaporized Te is supplied from the upstream side of the furnace. The CVD tellurization reaction occurs at 400 °C at which the vaporized Te lowers the melting temperature of Pt by eutectic formation, enabling the growth of 2D $PtTe_2$ layers [28,29]. This CVD tellurization method can grow wafer-scale 2D $PtTe_2$ layers of controlled thickness, as shown in Fig. 1b, which shows a sample of 2D $PtTe_2$ layers on a SiO_2/Si wafer on an area of ~12 cm^2. The thickness of as-grown 2D $PtTe_2$ layers was measured with the AFM characterization collaborated with cross-sectional TEM imaging. The plots in Fig. 1c correlate the thickness of initially deposited-Pt films vs. resulting 2D $PtTe_2$ layers, revealing high linearity indicating ~5 times thickness increase after the CVD tellurization. For convenience, 2D $PtTe_2$ samples are labeled by the thickness of Pt films; e.g., Pt $PtTe_2$-1nm denotes the sample prepared with Pt films of 1 nm thickness. The surface roughness of as-grown 2D $PtTe_2$ layers was also determined using AFM characterization. Representative AFM topography images of $PtTe_2$-0.5nm and $PtTe_2$-6nm samples are presented in Supporting Information, Fig. S1, confirming very small roughness values of ~0.7 and ~1.89 nm, respectively. Raman spectroscopy was used to investigate the spatial and chemical uniformity of the sample shown in Fig. 1b, where the color-marked four different spots were inspected. Two characteristic Raman peaks were observed, as presented in Fig. 1d, i.e., E_g peak at 117 c-1 and A_{1g} peak at 159 cm^{-1} corresponding to the in-plane and out-of-plane vibration modes of 2D P_2, respectively. The results are consistent with previous studies on single-crystal 2D $PtTe_2$ layers of much smaller dimensions (e.g., typically, a few μm2) [5,6,30]. Also, each spectrum exhibits nearly identical intensity ratio of Eg/A1g and peak positions irrespective of the different probe locations, suggesting the high uniformity of the sample. Energy-dispersive X-ray spectroscopy (EDS) in TEM was employed to analyze the spatial distribution of constituting elements and quantify their atomic concentrations. Fig. 1e presents the cross-sectional EDS elemental mapping images of a $PtTe_2$-1.5nm sample, confirming the highly uniform distribution of both Pt and Te. Fig. 1f shows the corresponding EDS spectrum, which identifies the atomic concentration of

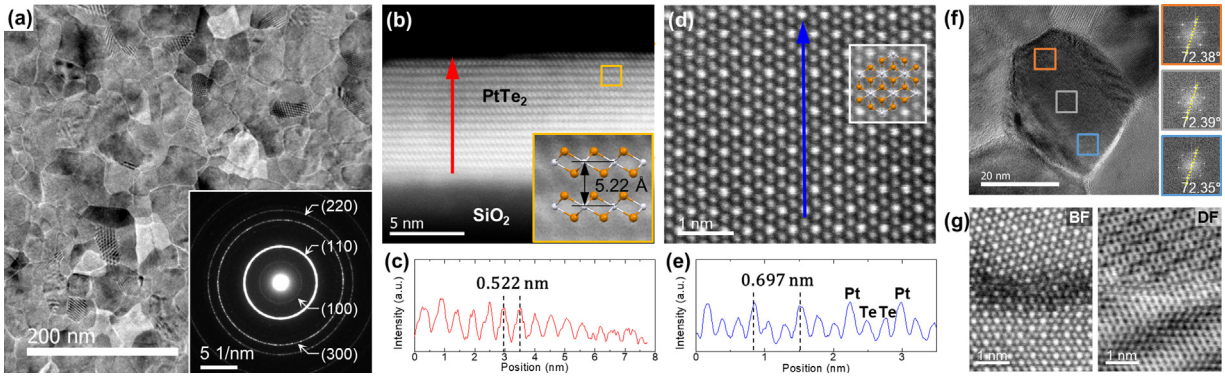

Fig. 2. (a) Plane-view HRTEM image of 2D $PtTe_2$ layers and the corresponding SAED pattern in the inset. (b) Cross-sectional HR-STEM image of 2D $PtTe_2$ multilayers along with the detailed atomic structure model in the inset. (c) Digital micrograph line intensity profile obtained along the red line in (b), indicating the interlayer distance of 5.22 Å. (d) Plane-view HR-STEM image of single-crystalline 2D $PtTe_2$ layers revealing 1T-phased structure. (e) Digital micrograph line intensity profile obtained along the blue line in (d), indicating the alternating location of Pt and Te atoms. (f) The HRTEM image of multi-grained 2D $PtTe_2$ layers. The inset images show FFT patterns corresponding to the square marked regions of the HRTEM image. (g) HR-STEM images of identical 2D $PtTe_2$ layers revealing the grain boundary obtained in BF and DF modes.

Pt:Te = 32.8:67.2 (i.e., 1:2.04), confirming the growth of stoichiometric 2D PtT2 layers.

The atomic structure and crystallinity of 2D $PtTe_2$ layers were thoroughly identified by scanning transmission electron microscope (STEM). Fig. 2a shows a representative dark-field STEM image of 2D $PtTe_2$ layers, revealing their polycrystalline structure. The entire sample is composed of multiple crystalline grains of distinct crystallographic orientational angles, and each grain consists of horizontally-aligned 2D $PtTe_2$ multilayers. The inset image is the selected area electron diffraction (SAED) pattern corresponding to the STEM image, revealing the dominant appearance of (100) and (110) crystalline planes. The SAED analysis indicates that 2D $PtTe_2$ layers are horizontally aligned, exposing their hexagonal basal planes parallel to the growth substrate surface. XRD characterization confirms that (001) crystalline peaks are dominantly observed in the same sample, further confirming the horizontally-aligned orientation of 2D $PtTe_2$ basal planes (Supporting Information, Fig. S2a). In addition, X-ray photoelectron spectroscopy (XPS) characterization identifies that the chemical composition of 2D $PtTe_2$ layers is nearly identical regardless of their thickness. (Supporting Information, Figs. S2b and c). Fig. 2b shows a high-resolution STEM (HR-STEM) image of 2D $PtTe_2$ multilayers possessing ~15 layers with a cross-sectional view, clearly revealing their horizontally-aligned orientation and evenly-spaced vdW gaps without any discontinuity. Fig. 2c shows a digital micrograph line intensity profile corresponding to the red arrow denoted in Fig. 2b, indicating the highly uniform interlayer spacing of ~5.22 Å, which corresponds to the 1T phase of hexagonal $PtTe_2$ [6]. The corresponding atomic structure illustration of stacked 1T-phased 2D $PtTe_2$ layers is provided in the inset of Fig. 2b. Fig. 2d shows a representative plane-view HR-STEM image of 2D $PtTe_2$ layers, further clarifying their 1T phase structure. The overlaid atomic structure model obtained by simulation indicates an octahedral configuration in which one centered Pt atom is coordinated with six Te atoms, corresponding to the crystalline structure of CdI_2-type 2D layers [6]. The line intensity profile in Fig. 2e corresponds to the blue arrow in Fig. 2d, and the intensity variation along the line indicates a periodic repetition of two Te atoms (lower intensity) in between one Pt atom (higher intensity). The distance between each Pt atom is measured to be 0.697 nm, which well agrees with previous studies [5,6]. We investigated the crystallinity of individual 2D $PtTe_2$ grains shown in Figs. 2a and 2f shows a representative HRTEM image of some grains. Compared to other Pt-based 2D TMD, such as $PtSe_2$ grown by the similar thermal selenization method, these 2D $PtTe_2$ layers contain a large number of individual grains accompanying well-defined grain boundaries and sharp interfaces [1]. The images on the right panel of Fig. 2f present a series of fast Fourier transform (FFT) corresponding to the color-boxed regions in the HRTEM image. The deviation of angles with respect to the orientation of each diffraction spot in the FFT patterns is less than 0.1°, indicating that the 2D $PtTe_2$ grain consists of a large single grain. Additional dark-field HR-STEM image and four different FFT patterns obtained from the same sample are presented in Supporting Information, Fig. S3a, further confirming that the 2D $PtTe_2$ layer possesses a polycrystalline structure composed of multiple grains with random orientations. The lateral dimensions of the crystalline grains in Fig. 2a are approximated by image analysis, and the average value for their equivalent diameters (= 4 × Area/Perimeter) is determined to be 28.4 ± 9.2 nm (Supporting Information, Fig. S3b). Fig. 2g presents representative HRTEM images of two adjacent crystalline grains across a grain boundary in bright-field (BF: left) and dark-field (DF: right) views, respectively. It is evident that the grain boundary contains a large number of vacancies owing to the misalignment of each grain, which reveals Moiré patterns with diverse fringe orientations – pronouncedly visible in the DF image. The observation of such Moiré fringe patterns indicates that each grain is composed of vertically-stacked 2D $PtTe_2$ multilayers whose basal planes misaligned along [001] zone axis.

3.2. Electrical and electrothermal properties of 2D $PtTe_2$ layer

Before investigating the electrothermal performances of 2D $PtTe_2$ layers in mechanically stretchable forms, we first studied their electrical conductivities. Fig. 3a presents the thickness-dependent sheet resistance (R_s) of 2D $PtTe_2$ layers obtained with Pt films of varying thicknesses. R_s values steadily decrease with increasing Pt thickness, and the $PtTe_2$-9 nm sample exhibits a value as low as 19.4 Ω/□. This value is quite lower than those of other electrothermal nanomaterials previously developed for stretchable heaters; e.g., 43 Ω/□ for doped multilayer graphene, and 215 Ω/□ for MXene based composites [24,27]. Such low R_s values are essential for efficient electrothermal energy conversion as the Joule-heating efficiency is expressed by $P = V^2/R_s$, where P is power and V is voltage [25,27]. Moreover, the low R_s values should be maintained even in a wide range of high temperature under actual operating conditions, which is essential for reliable and practical electrothermal device applications. Fig. 3b shows temperature-dependent R_s values normalized to that obtained at room temperature ($R_{s,RT}$), revealing that they are nearly unchanged (< 0.1% degradation) even up to 225 °C. Unlike most of the metal-based heaters that suffer from resistivity degradation

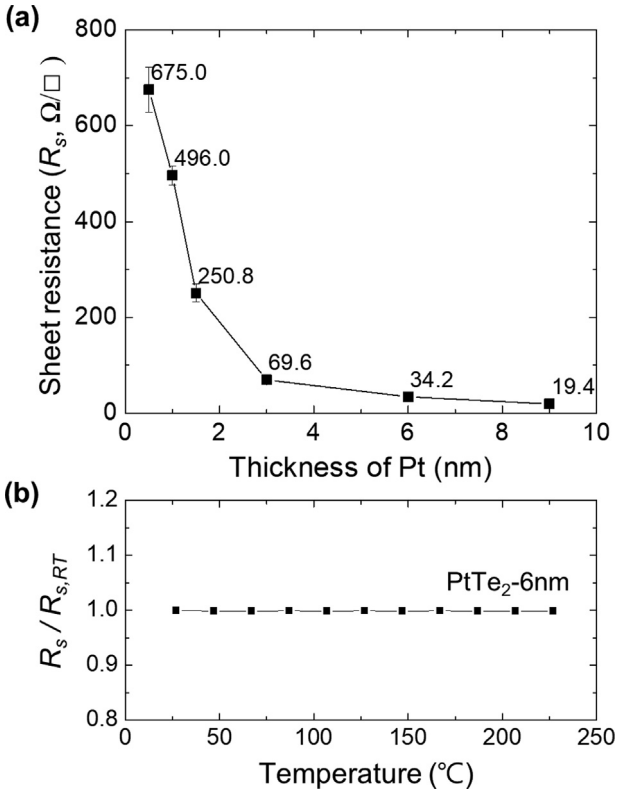

Fig. 3. (a) Sheet resistances of 2D $PtTe_2$ layers prepared with Pt films of various thicknesses. (b) The temperature-dependent ratio of sheet resistance (R_s) normalized to the room-temperature sheet resistance ($R_{s,RT}$) obtained from $PtTe_2$-6nm sample.

with increasing temperature, 2D $PtTe_2$ layers exhibit very stable temperature-invariant electrical properties [31]. These combined attributes of intrinsically superior electrical conductivity and thermal stability coupled with the low CVD growth temperature (i.e., 400 °C) of 2D $PtTe_2$ layers make them a promising candidate for high-performance mechanically stretchable heaters.

To pursue this projected opportunity, we first demonstrated the direct growth of 2D $PtTe_2$ layers on mechanically flexible PI substrates. By applying the identical CVD recipe adopted for SiO_2/Si as growth substrates, we grew 2D $PtTe_2$ layers on PI substrates which are highly stable even above 400 °C [1]. XPS characterization confirmed that the Pt 4f and Te 3d core-energy spectral peaks and positions are nearly identical for 2D $PtTe_2$ layers grown on both PI and SiO_2/Si substrates (Supporting Information, Fig. S4), confirming the generality of our CVD method. Fig. 4a shows optical images of as-grown 2D $PtTe_2$ layers on PI substrates prepared with Pt films of varying thickness, revealing decreasing optical transparency with increasing thickness. Electrothermal properties of these samples were characterized by identifying their temperature variation upon an application of electrical biasing, determined by IR imaging. Fig. 4b presents a diagram that correlates the maximum temperature (T_{max}) of 2D $PtTe_2$/PI samples prepared with varying Pt thickness obtained at three different applied voltages. T_{max} steadily increases with increasing thicknesses due to lower sheet resistance (Fig. 3a) as predicted by the Joule-heating efficiency equation ($P = V^2/R_s$). Indeed, we note that the electrically-driven temperature change of these samples well follows the Joule-heating efficiency equation irrespective of their thickness, as presented in Supporting Information, Fig. S5a. Particularly, we observe that these 2D $PtTe_2$/PI heaters exhibit significantly high temperature even at very low operation voltages, e.g., ~170 °C for $PtTe_2$-9 nm at 7 V, much lower than the voltage regarded as non-hazardous according to International Electrotechnical Commission (IEC 60950-1) [32]. Fig. 4c shows the time-dependent variation of T_{max} for 2D $PtTe_2$ layers prepared with varying Pt thickness operated at a constant voltage of 5 V for 30 sec. Upon the on-set/termination of the voltage denoted by the first/second dashed lines, respectively, T_{max} rapidly increases/decreases within 10 secs for all samples. Fig. 4d presents the first derivatives of the time-temperature plots in Fig. 4c, clarifying the heating/cooling kinetics of the 2D $PtTe_2$ layers more precisely. The $PtTe_2$-9nm sample exhibits the heating/cooling rate of 26.6 °C/sec and 24.2 °C/sec under 5 V, respectively, which allows the heater to reach T_{max} much faster (5 sec) than that obtained with other nanomaterials previously explored for heater applications; e.g., nano graphite [33], or reduced graphene oxide (rGO) [34], as summarized in Table 1. These heating/cooling rates can be further increased to 46.8 °C/sec and 36.6 °C/sec by applying a higher voltage of 7 V, respectively, achieving significantly faster thermal responses - Supporting Information, Figs. S5b-e. Moreover, we also evaluated the electrothermal endurance of these samples by applying/terminating a constant voltage in a cyclic manner and identifying resulting temperature variation. The plot of cycle number vs. temperature in Fig. 4e presents the cyclic heating/cooling of an identical sample (i.e., 2D $PtTe_2$-6nm) obtained under a cyclic application/termination of 4 V for 50 times. Considering the fast heating/cooling rate of the sample for achieving T_{max}/ambient temperature, a fixed interval of 10 sec was assigned for the voltage application/termination in each cycle. It is noteworthy that the average T_{max} of 81.9 °C is well retained throughout the entire cyclic period accompanying a very small deviation of ~1.0 °C, confirming excellent electrothermal endurance essential for practical applications. Fig. 4f presents IR images of the same sample in Fig. 4e, obtained at specific periods of 1st, 25th, and 50th cycles, showing the stable operation with multiple cycles. Furthermore, in a way to assess the technological potential of 2D $PtTe_2$/PI materials as a portable heater for practical applications, we characterized their electrothermal performances driven by solar energy. Fig. 4g shows a representative image (left) of a 2D $PtTe_2$-6nm sample connected to a portable solar panel and its corresponding IR images without (mid) and with (right) sunlight illumination. Fig. 4h presents the variation of temperature for the samples of various thickness operated at ~4 V driven by solar energy. (Air mass: ~1.3, Ambient temperature ~30 °C) It is noteworthy the 2D $PtTe_2$-6nm sample reaches T_{max} of 53.0 °C in its ON state (with illumination), which is > ~25 °C increase compared to its OFF state (without illumination). All these results comprehensively indicate that 2D $PtTe_2$ layers possess a large set of electrothermal properties essential for high-performance heating devices; i.e., low operational voltage, rapid responsiveness as well as high thermal stability and endurance.

3.3. Flexibility of 2D $PtTe_2$ layer

Having confirmed the intrinsically suitable properties of 2D $PtTe_2$ layers, we then explored their opportunity for mechanically flexible and stretchable heaters towards personalized wearable technologies. In designing such devices, we have to consider the human body motions of various forms, e.g., stretching, bending, rotating, and folding at joints [35], and their influences on resulting device performances. We first evaluated the electrothermal properties of 2D $PtTe_2$ layers undergoing a simple mechanical bending by using the 2D $PtTe_2$-6nm/PI sample as a representative case (PI thickness is 50 μm). Prior to the experimental evaluation, we carried out FEM calculations that simulate the bending of 2D $PtTe_2$-6nm/PI with different bending radius (r) and angle (α), as shown in Supporting Information, Fig. S6. The FEM results show that the $PtTe_2$ layers experience a tensile or compressive strain during the outward (Figs. S6a and b) or inward (Figs. S6c and d) bending sit-

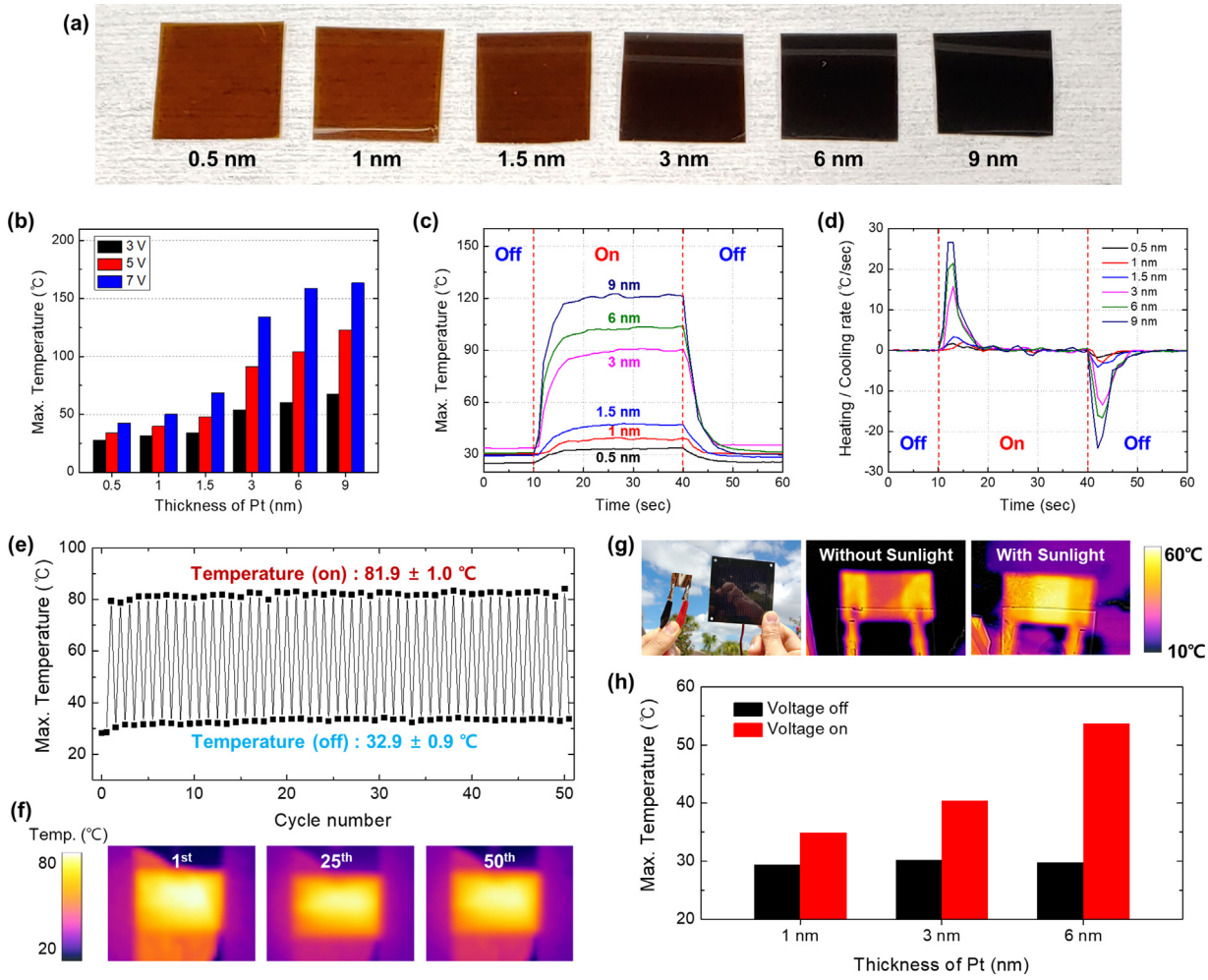

Fig. 4. (a) Photos of 2D $PtTe_2$ layers-grown flexible PI substrates prepared with Pt films of various thicknesses. (b) The maximum temperature of 2D $PtTe_2$/PI samples prepared with various Pt thickness achieved at biases of 3, 5, and 7 V. (c) Time-dependent temperature fall/rise of the same samples in (b) obtained at 5 V. (d) Determination of the heating/cooling rate corresponding to (c). (e) Temperature variation obtained from a 2D $PtTe_2$-6nm/PI sample during the cyclic heating/cooling of 50 times at 4 V. (f) Representative IR images of the sample in (e) at three different cycle numbers. (g) Demonstration of the solar energy-driven operation of 2D $PtTe_2$/PI heaters. (h) Temperature variations achieved with 2D $PtTe_2$/PI heaters of various thickness driven by solar energy.

Table 1
Comparison of the electrothermal performance and the flexibility with the recently developed nanomaterial-based wearable heaters.

Material	T_{max} (°C)/Voltage (V)	Time required for T_{max}	Flexibility	Ref.
Cu/PI	95 °C/3.8 V	2 sec	Bendable, Stretchable (800%)	[39]
Liquid-metal/PDMS	90 °C/3.5 V	> 180 sec	Stretchable (100%)	[38]
Ag dendrites/PET	135 °C/4 V	35 sec	Bendable	[42]
Graphite/PVC	35 °C/5 V	30 sec	Bendable	[43]
Graphite nanoplatelet/PI	50 °C/6 V	~ 100 sec	Bendable	[33]
rGO/PI	86 °C/9 V	~ 10 sec	Bendable	[34]
Ag + rGO/PI	70 °C/9 V	~ 5 sec	Bendable	[26]
Ag NW + SWCNT/PDMS	87 °C/5 V	~ 120 sec	Bendable, Stretchable (~50%)	[12]
MXene/PET	35 °C/5 V	~ 40 sec	Bendable	[27]
2D $PtTe_2$/PI	120 °C/5 V	5 sec	Bendable	This
	58 °C/5 V	5 sec	Stretchable (~130%)	work

uations, respectively. The amount of the strain increases with decreasing the bending radius as well as increasing the bending angle irrespective of bending orientation. Meanwhile, it is insensitive to the bending orientation given the bending radius/angle of an identical value. We experimentally evaluated the electrothermal performance of the sample by measuring its temperature and resistance changes under outward bending, circumventing any noticeable degradation caused by crack generation [36]. Fig. 5a presents IR images of the sample subjected to the mechanical deformation of controlled bending angle from 0° to 180°, which are viewed in a top-to-bottom orientation. It is noted that the sample does not exhibit any significant performance degradation manifested by temperature reduction even under the bending up to 180°, measured with a bending radius of 2 mm at 3 V. The inset in Fig. 5b presents the side-view schematic illustration of the sample corresponding to Fig. 5a, defining measurement parameters of bending angle (α) and radius (r). Fig. 5b presents the change of T_{max} (top panel) and normalized resistance, R/R_o, where R_o denotes the resistance at un-

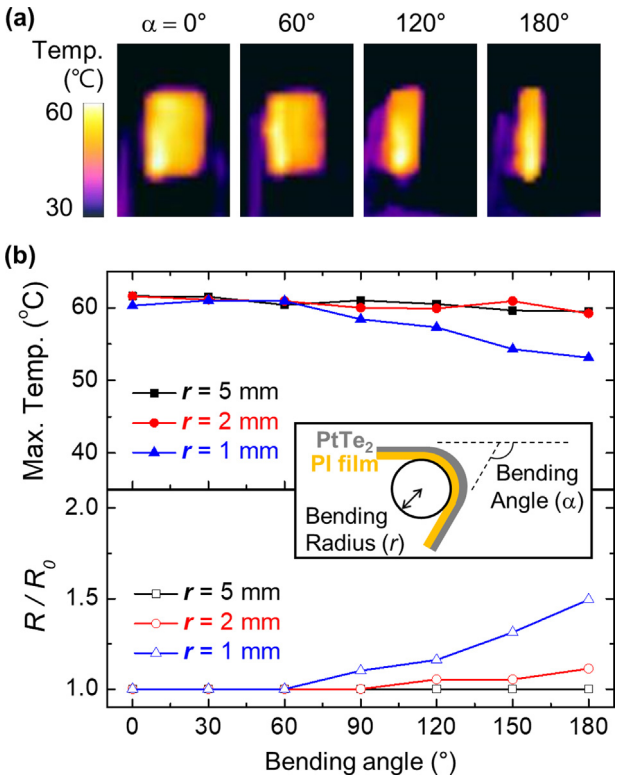

Fig. 5. (a) IR images of a $PtTe_2$-6nm/PI sample at various bending angles obtained with the bending radius of 2 mm at 3 V. (b) Variation of the maximum temperature and relative resistance for the same sample in (a) as a function of bending angle and bending radius.

bent state (bottom panel) as a function of bending angle (α) and radius (r). It is rational to assume that smaller bending radii and larger bending angles would lead to more significant deformation in 2D $PtTe_2$ layers as their outward surface will experience high mechanical tension. Indeed, the plots in Fig 5b confirms a significant increase in R/R_0 and decrease in T_{max} with increasing bending angles, noticeably observed with the sample with a small bending radius of 1 mm (2.3% of tensile strain, Fig. S6b). However, with a larger bending radius of 5 mm (0.5% of tensile strain, Fig. S6b), such a significant change is not observed in both R/R_0 and T_{max} even under deformation up to the bending angle of 180°.

This observation confirms that 2D $PtTe_2$ layers do not undergo any significant structural degradation even under a large extent of mechanical deformation, preserving their intrinsic property advantages. With consideration of the realistic deformation range in human body joints, the results are highly encouraging for the application of 2D $PtTe_2$ layers in wearable and attachable heater devices for personalized applications.

3.4. Kirigami-patterned stretchable heater based on 2D $PtTe_2$

Encouraged by these intrinsically superior electrothermal properties and deformation-insensitive structural integrity inherent to 2D $PtTe_2$ layers, we set on exploring them for skin-attachable flexible heaters. To this end, it is particularly essential to configure the 2D $PtTe_2$/PI heaters in mechanically stretchable forms well to suit the demands of complex human body motions. Notably, recent studies suggested that stretchability up to at least 70% is demanded to accommodate maximum human body linear elongation into wearable device technologies [12,37]. Various strain engineering schemes employing judiciously designed patterns and structures have been explored to achieve strain-invariant properties in stretchable devices, which includes wavy [38], island-interconnect [39], and Kirigami geometries [2,40,41]. Adopting these pattern-based strategies to the wearable heater application, we developed strain-invariant 2D $PtTe_2$/PI heaters by employing the concept of Kirigami pattern designing and evaluated their electrothermal performances under varying stretch levels. Kirigami patterning approaches inspired the ancient paper-cutting arts have been employed to efficiently relieve externally applied tensile stress within 2D objects by converting it to 3D torsional stress. Fig. 6a shows the schematic illustration of fabrication procedures for Kirigami-patterned 2D $PtTe_2$/PI stretchable heaters. Kirigami patterns containing periodic uni-directional cuts were fabricated on a PI substrate by a mechanical cutting machine, which was designed to accommodate large stretchability [2]. Subsequently, Pt was deposited on the patterned PI, followed by the above described CVD thermal tellurization, which yielded the Kirigami-patterned 2D $PtTe_2$/PI. Lastly, gold (Au) electrodes were deposited on both ends of the Kirigami-patterned 2D $PtTe_2$/PI for electrical measurements under mechanical stretching. A simple Kirigami pattern composed of periodic straight cut lines perpendicular to stretching direction was adopted in this work. Fig. 6b illustrates the schematic of the corresponding Kirigami pattern specifying geometrical parameters; a is the length of the cut, b is the spacing between two cuts in the transverse direction, and c is the spacing in the longitudinal direction. In this model, the critical tensile force (F) accommodated by the Kirigami pattern is expressed as follows; [2]

$$F \propto Ec/(a-b)^3 \quad (1)$$

where E is Young's modulus of the Kirigami material. The Eq. (1) implies that F should decrease by decreasing c and increasing $a-b$, indicating that the pattern can accommodate larger strain without distortion. To clarify the above predicted dimensional effects on resulting stretchability, we conducted the FEM simulation to quantify the spatial distribution of maximum in-plane principal strain, ε_{max}, within our Kirigami device upon a simulated tensile strain. We then experimentally measured the tensile strain-driven variation of electrical resistance and compared the results to the FEM simulation predictions. The top panels in Figs. 6c-e present the FEM simulations predicting the variation of ε_{max} within the Kirigami pattern as a function of longitudinal tensile strain for three different cases of varying a, b, and c. The bottom panels in Figs. 6c-e show the experimentally determined variation of resistance (R), which were measured with $PtTe_2$-9nm based Kirigami heater, corresponding to the top-panel FEM simulations for each case. At first, we compare the trend of ε_{max} and R change with/without creating the Kirigami pattern corresponding to Fig. 6b, which is defined by $a = 15$ mm, $b = 3$ mm, and $c = 3$ mm. As shown in Fig. 6c, the 2D object without the Kirigami pattern exhibits significantly high ε_{max} in the entire area upon applying the longitudinal tensile strain (top panel), which is manifested by significantly increasing R with the increasing strain (bottom panel). By introducing the above-defined Kirigami pattern into the same object, we achieve nearly strain-invariant mechanical deformation and electrical responses, i.e., an insignificant increase of ε_{max} (top panel) and R (bottom panel) even up to the tensile strain of ~120 %. This analysis indicates that incorporation of judiciously designed Kirigami patterns can introduce remarkably improved stretchability into our 2D $PtTe_2$/PI heaters without compromising their intrinsic electrothermal superiority.

We further investigated the strain-invariant mechanical and electrical responses of our Kirigami patterns by systematically varying the geometrical parameters. In Fig. 6d, we compare the FEM simulation of ε_{max} with the experimentally determined R while varying $a-b$ values (unit of mm) while keeping $c = 3$ mm constant. As the Eq. (1) predicts, we note that the mechanical stretchability of the Kirigami pattern steadily increases with in-

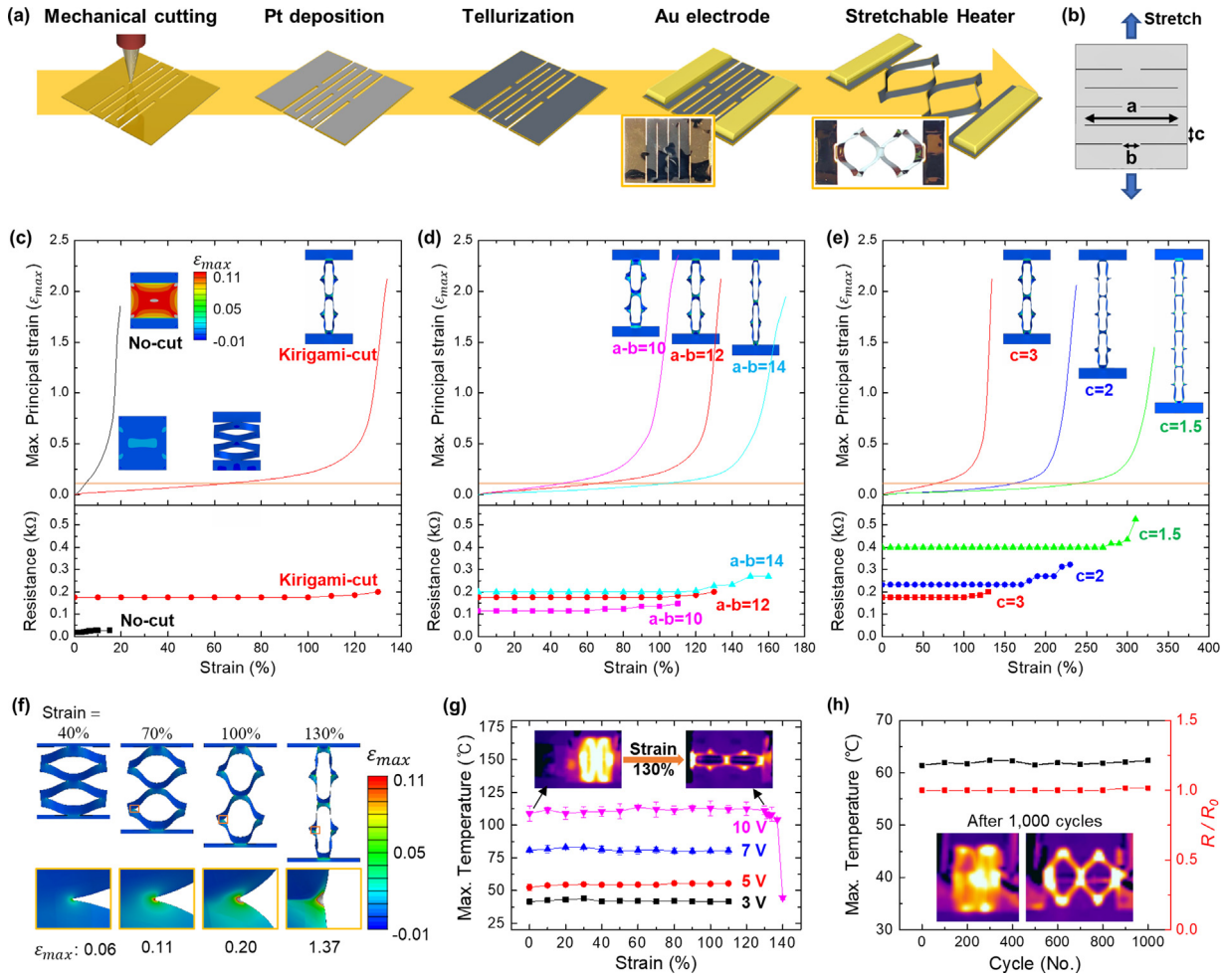

Fig. 6. (a) Schematic illustrations for the fabrication process of Kirigami-patterned 2D $PtTe_2$ layers-based stretchable heater. The insets show representative images of a fabricated heater before/after stretching. (b) Sketch of the Kirigami pattern adopted in this experiment defining the geometrical parameters of *a*, *b*, and *c*. (c-e) Comparisons of strain-invariant mechanical deformations predicted by FEM simulations (top panels) and electrical responses confirmed by experiments (bottom panels) in various in Kirigami patterns; (c) Comparison between with/without Kirigami patterns, (d) Comparison with varying $a-b$ and constant *c*. (e) Comparison with varying *c* and constant $a-b$. (f) FEM simulation images showing the spatial distribution of in-plane principal strain in a Kirigami pattern at various stretch levels. (g) IR images of a 2D $PtTe_2$/PI Kirigami heater (insets) and the corresponding plots of T_{max} vs. strain rate for various applied voltages. (h) Variations of T_{max} and R/R_0 obtained from the same sample in (g) during the cyclic stretch of 1,000 times with 70% of strain.

creasing $a-b$ (top panel), which leads to improved strain-invariant electrical responses (experimental bottom panel). We also identify similar trends by systematically increasing c while keeping $a-b$ constant, as shown in Fig. 6e. It is worth mentioning that we observe that the experimentally demonstrated electrical responses of our Kirigami patterns well agree with the FEM simulation-based predictions throughout Figs. 6d-e; i.e., the onsets of ε_{max} (FEM) and R (experiments) increase are observed at nearly identical strain % values. For instance, for the case of $c = 1.5$ mm in Fig. 6e, both ε_{max} and R drastically increase at a strain value of ~300 %. This high coherency of simulations vs. experiments indicates that our Kirigami fabrication approach (Fig. 6a) ensures high controllability and accuracy of pattern definition. Considering the linear elongation ratio of any human body motions is limited to ~70% [12,37], we have judiciously selected the geometrical parameters to be $a = 15$ mm, $b = 3$ mm, and $c = 3$ mm and incorporated them into our Kirigami devices for electrothermal demonstrations. Note that these parameters are anticipated to ensure the stable operation of the Kirigami devices up to ~130 % strain (the red plot in the bottom panel of Fig. 6d), which is to be verified as follows. Fig. 6f presents the FEM global strain map images detailing the spatial distribution of ε_{max} within the Kirigami pattern defined by the above geometrical parameters as a function of tensile strain levels. With increasing tensile strain levels, the Kirigami pattern steadily undergoes a transition from 2D in-plane to 3D out-of-plane deformation involving the twist of the pattern cut edges. It is visualized that internal strain is gradually developed and concentrated on the cut edges (orange boxes) with increasing tensile strain levels; e.g., ε_{max} remains ~0.11 until the tensile strain reaches ~70% and increases to ~0.2 with 100% strain, indicating its efficient relaxation through the 2D-to-3D structural deformation. Further stretching to the strain of 130% leads the ε_{max} to be 1.37, which is > 10 times than that observed at 70 %, indicating a significant concentration of partial strain at the cut edges. Detailed ε_{max} distribution and the out-of-plane deformation for each strain steps are summarized in Supporting Information, Fig. S7. We then experimentally demonstrated electrothermal performances of 2D $PtTe_2$/PI Kirigami heaters under varying tensile stretch conditions and compared them to the FEM predictions. The insets in Fig. 6g show the representative IR images of a Kirigami-patterned 2D $PtTe_2$-9nm/PI sample (initial size; 18×12 mm^2) in a range of 3 to 10 V under varying stretch levels. The plots in Fig. 6g show that the temperature of the corresponding Kirigami sample increases with increasing voltage, which is well retained up to 110 % strain at each applied voltage. For in-

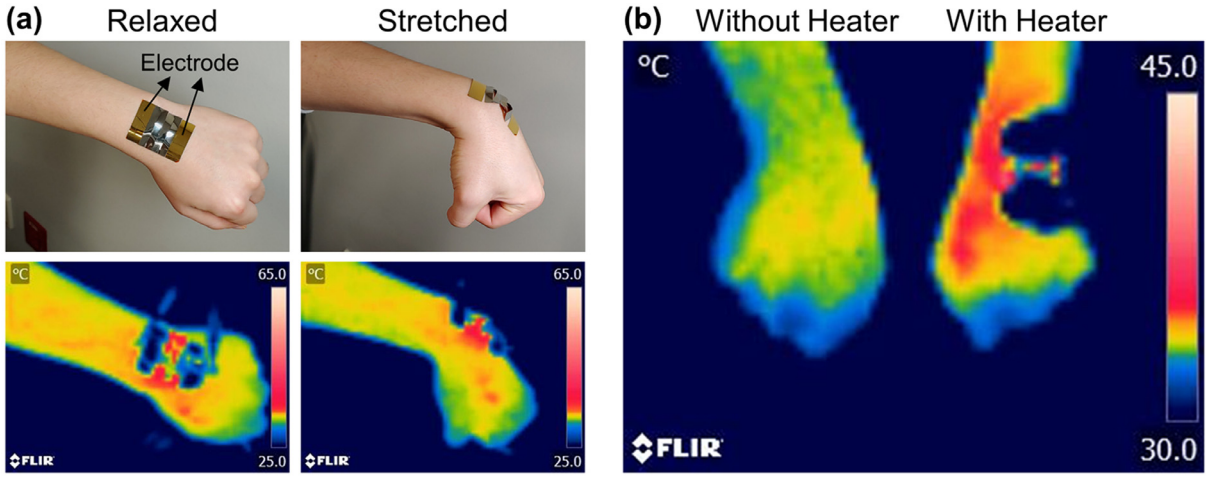

Fig. 7. (a) Demonstration of skin-attachable 2D PTe_2 layers-based Kirigami heaters in accordance with the mechanical motions of a human wrist. The IR images on the bottom panels show temperature distribution on the wrist when the heater was electrically biased. (b) IR images showing the temperature distribution of the wrists with (right) and without (left) attaching the heater.

stance, T_{max} of ~115 °C achieved by 10 V remains nearly constant up to ~ 130% of strain after which it drastically drops to ~44 °C as a result of mechanical fracture at the cut edges of the Kirigami pattern. Voltage-driven temperature variations of the same sample were also identified, as presented in Supporting Information, Fig. S8; e.g., a high heating rate of 22.4 °C/sec was observed to reach T_{max} of ~119.3 °C at 10 V. Next, we examined the durability and robustness of this 2D $PtTe_2$/PI Kirigami heater by repeatedly applying/releasing a fixed tensile stain in a cyclic manner. Fig. 6h shows the plots of T_{max} and R/R_0 obtained from the same sample during the course of 1,000 cycles at 70% strain under 7 V. It is observed that T_{max} varies within ± 1 °C and R/R_0 slightly increases by less than 2% after the 1,000 times cyclic stretching, indicating its outstanding fatigue tolerance.

Lastly, we demonstrated the applicability of our 2D $PtTe_2$/PI Kirigami devices for skin-attachable wearable heaters. Fig. 7a shows the optical images (top panel) and the corresponding IR images (bottom panel) of a large 2D $PtTe_2$/PI Kirigami heater (size: 36 × 24 mm^2) attached to a wrist undergoing realized and stretched motions. The images confirm the excellent attachability and stretchability of the Kirigami heater, which well performs even integrated on the highly curved surface in dynamic motions of the human body. Fig. 7b compares the IR images of the wrist with and without the Kirigami heater operated at 10 V, revealing a temperature difference of > 10 °C.

4. Conclusions

In summary, we explored wafer-scale CVD-grown 2D $PtTe_2$ layers for high-performance mechanically deformable heaters by employing their intrinsically superior mechanical, electrical, and thermal properties. CVD-2D $PtTe_2$ layers directly grown on large PI substrates at 400 °C exhibited excellent Joule heating efficiency – i.e., the fast rise of high temperature at a given voltage – superior to those of previously explored all other state-of-the-art nanomaterials. Furthermore, we prepared for them in the form of judiciously-designed Kirigami patterns and demonstrated high-performance skin-attachable heaters, which exhibited strain invariant electrothermal properties and large stretchability. This study confirms the high promise of these emerging metallic 2D layered materials for a wide range of futuristic stretchable device technologies.

ASSOCIATED CONTENT

Supporting Information. Additional characterization data including AFM, XRD, XPS, TEM, FEM simulation, and plots of bias-dependent temperature variation. The Supporting Information is available free of charge on the web.

Declaration of interests

The authors declare that they have no known competing financial interests or personal relationships that could have appeared to influence the work reported in this paper.

CRediT authorship contribution statement

Tae-Jun Ko: Methodology, Investigation, Writing - original draft. **Sang Sub Han:** Investigation, Visualization. **Emmanuel Okogbue:** Investigation, Methodology. **Mashiyat Sumaiya Shawkat:** Formal analysis, Investigation. **Mengjing Wang:** Formal analysis, Investigation. **Jinwoo Ma:** Formal analysis. **Tae-Sung Bae:** Formal analysis. **Shihab Bin Hafiz:** Formal analysis. **Dong-Kyun Ko:** Methodology, Investigation. **Hee-Suk Chung:** Formal analysis, Investigation. **Kyu Hwan Oh:** Conceptualization. **Yeonwoong Jung:** Conceptualization, Supervision, Project administration, Writing - review & editing.

ACKNOWLEDGMENT

This work was supported by the National Science Foundation (CMMI-1728390) (M.S.S., and Y. J.), the Korea Institute of Energy Technology Evaluation and Planning (KETEP) and the Ministry of Trade, Industry & Energy (MOTIE) of the Republic of Korea (No. 20173010013340) (Y.J.). Y. J. also acknowledges VPR Advancement of Early Career Researchers award from the University of Central Florida. This research was in part supported by the Creative Materials Discovery Program through the National Research Foundation of Korea (NRF) funded by the Ministry of Science, ICT and Future Planning (NRF-2019M3D1A1069793). Shihab B. Hafiz gratefully acknowledges his graduate student support from National Science Foundation (ECCS-1809112).

References

[1] S.S. Han, J.H. Kim, C. Noh, J.H. Kim, E. Ji, J. Kwon, S.M. Yu, T.-J. Ko, E. Okogbue, K.H. Oh, H.-S. Chung, Y. Jung, G.-H. Lee, Y. Jung, Horizontal-to-vertical tran-

sition of 2D layer orientation in low-temperature chemical vapor deposition-grown $PtSe_2$ and its influences on electrical properties and device applications, ACS Appl. Mater. Interfaces 11 (2019) 13598–13607 https://doi.org/10.1021/acsami.9b01078.
[2] E. Okogbue, S.S. Han, T.-J. Ko, H.-S. Chung, J. Ma, M.S. Shawkat, J.H. Kim, J.H. Kim, E. Ji, K.H. Oh, L. Zhai, G.-H. Lee, Y. Jung, Multifunctional two-dimensional $PtSe_2$-layer kirigami conductors with 2000% stretchability and metallic-to-semiconducting tunability, Nano Lett. 19 (2019) 7598–7607 https://doi.org/10.1021/acs.nanolett.9b01726.
[3] L. Pi, L. Li, K. Liu, Q. Zhang, H. Li, T. Zhai, Recent progress on 2D Noble-transition-metal dichalcogenides, Adv. Funct. Mater. 29 (2019) 1904932 https://doi.org/10.1002/adfm.201904932.
[4] R.A.B. Villaos, C.P. Crisostomo, Z.-Q. Huang, S.-M. Huang, A.A.B. Padama, M.A. Albao, H. Lin, F.-C. Chuang, Thickness dependent electronic properties of Pt dichalcogenides, npj 2D Mater. Appl. 3 (2019) 2 https://doi.org/10.1038/s41699-018-0085-z.
[5] L. Fu, D. Hu, R.G. Mendes, M.H. Rummeli, Q. Dai, B. Wu, L. Fu, Y. Liu, Highly organized epitaxy of dirac semimetallic $PtTe_2$ crystals with extrahigh conductivity and visible surface plasmons at edges, ACS Nano 12 (2018) 9405–9411 https://doi.org/10.1021/acsnano.8b04540.
[6] S. Hao, J. Zeng, T. Xu, X. Cong, C. Wang, C. Wu, Y. Wang, X. Liu, T. Cao, G. Su, L. Jia, Z. Wu, Q. Lin, L. Zhang, S. Yan, M. Guo, Z. Wang, P. Tan, L. Sun, Z. Ni, S.-J. Liang, X. Cui, F. Miao, Low-temperature eutectic synthesis of $PtTe_2$ with weak antilocalization and controlled layer thinning, Adv. Funct. Mater. 28 (2018) 1803746 https://doi.org/10.1002/adfm.201803746.
[7] M. Wang, T.-J. Ko, M.S. Shawkat, S.S. Han, E. Okogbue, H.-S. Chung, T.-S. Bae, S. Sattar, J. Gil, C. Noh, K.H. Oh, Y. Jung, J.A. Larsson, Y. Jung, Wafer-scale growth of 2D $PtTe_2$ with layer orientation tunable high electrical conductivity and superior hydrophobicity, ACS Appl. Mater. Interfaces 12 (2020) 10839–10851 https://doi.org/10.1021/acsami.9b21838.
[8] A. Favron, E. Gaufrès, F. Fossard, A.-L. Phaneuf-L'Heureux, N.Y.W. Tang, P.L. Lévesque, A. Loiseau, R. Leonelli, S. Francoeur, R. Martel, Photooxidation and quantum confinement effects in exfoliated black phosphorus, Nat. Mater. 14 (2015) 826–832 https://doi.org/10.1038/nmat4299.
[9] J.O. Island, G.A. Steele, H.S.J.v.d. Zant, A. Castellanos-Gomez, Environmental instability of few-layer black phosphorus, 2D Mater. 2 (2015) 011002 https://doi.org/10.1088/2053-1583/2/1/011002.
[10] L. Tan, M. Zeng, Q. Wu, L. Chen, J. Wang, T. Zhang, J. Eckert, M.H. Rummeli, L. Fu, Direct growth of ultrafast transparent single-layer graphene defoggers, Small 11 (2015) 1840–1846 https://doi.org/10.1002/smll.201402427.
[11] E. Okogbue, T.-J. Ko, S.S. Han, M.S. Shawkat, M. Wang, H.-S. Chung, K.H. Oh, Y. Jung, Wafer-scale 2D $PtTe_2$ layers for high-efficiency mechanically flexible electro-thermal smart window applications, Nanoscale (2020) https://doi.org/10.1039/D0NR01845G.
[12] H. Kim, M. Seo, J.W. Kim, D.K. Kwon, S.E. Choi, J.W. Kim, J.M. Myoung, Highly stretchable and wearable thermotherapy pad with micropatterned thermochromic display based on Ag nanowire–single-walled carbon nanotube composite, Adv. Funct. Mater. 29 (2019) 1901061 https://doi.org/10.1002/adfm.201901061.
[13] Y. Guo, C. Dun, J. Xu, J. Mu, P. Li, L. Gu, C. Hou, C.A. Hewitt, Q. Zhang, Y. Li, D.L. Carroll, H. Wang, Ultrathin, washable, and large-area graphene papers for personal thermal management, Small 13 (2017) 1702645 https://doi.org/10.1002/smll.201702645.
[14] J. Ahn, J. Gu, B. Hwang, H. Kang, S. Hwang, S. Jeon, J. Jeong, I. Park, Printed fabric heater based on Ag nanowire/Carbon nanotube composites, Nanotechnology 30 (2019) 455707 https://doi.org/10.1088/1361-6528/ab35eb.
[15] S. Yao, J. Cui, Z. Cui, Y. Zhu, Soft electrothermal actuators using silver nanowire heaters, Nanoscale 9 (2017) 3797–3805 https://doi.org/10.1039/C6NR09270E.
[16] P. Mostafalu, A. Tamayol, R. Rahimi, M. Ochoa, A. Khalilpour, G. Kiaee, I.K. Yazdi, S. Bagherifard, M.R. Dokmeci, B. Ziaie, S.R. Sonkusale, A. Khademhosseini, Smart bandage for monitoring and treatment of chronic wounds, Small 14 (2018) 1703509 https://doi.org/10.1002/smll.201703509.
[17] T.-J. Ko, M. Wang, C. Yoo, E. Okogbue, M.A. Islam, H. Li, M.S. Shawkat, S.S. Han, K.H. Oh, Y. Jung, Large-area 2D TMD layers for mechanically reconfigurable electronic devices, J. Phys. D: Appl. Phys. 53 (2020) 313002 https://doi.org/10.1088/1361-6463/ab87bb.
[18] S. Hong, H. Lee, J. Lee, J. Kwon, S. Han, Y.D. Suh, H. Cho, J. Shin, J. Yeo, S.H. Ko, Highly stretchable and transparent metal nanowire heater for wearable electronics applications, Adv. Mater. 27 (2015) 4744–4751 https://doi.org/10.1002/adma.201500917.
[19] P. Lee, J. Ham, J. Lee, S. Hong, S. Han, Y.D. Suh, S.E. Lee, J. Yeo, S.S. Lee, D. Lee, S.H. Ko, Highly stretchable or transparent conductor fabrication by a hierarchical multiscale hybrid nanocomposite, Adv. Funct. Mater. 24 (2014) 5671–5678 https://doi.org/10.1002/adfm.201400972.
[20] P. Lee, J. Lee, H. Lee, J. Yeo, S. Hong, K.H. Nam, D. Lee, S.S. Lee, S.H. Ko, Highly Stretchable and highly conductive metal electrode by very long metal nanowire percolation network, Adv. Mater. 24 (2012) 3326–3332 https://doi.org/10.1002/adma.201200359.
[21] S.-P. Chen, Y.-C. Liao, Highly stretchable and conductive silver nanowire thin films formed by soldering nanomesh junctions, Phys. Chem. Chem. Phys. 16 (2014) 19856–19860 https://doi.org/10.1039/C4CP02808B.
[22] K. Chu, D.-J. Yun, D. Kim, H. Park, S.-H. Park, Study of electric heating effects on carbon nanotube polymer composites, Org. Electron. 15 (2014) 2734–2741 https://doi.org/10.1016/j.orgel.2014.07.043.
[23] H.H. Khaligh, L. Xu, A. Khosropour, A. Madeira, M. Romano, C. Pradére, M. Tréguer-Delapierre, L. Servant, M.A. Pope, I.A. Goldthorpe, The joule heating problem in silver nanowire transparent electrodes, Nanotechnology 28 (2017) 425703 https://doi.org/10.1088/1361-6528/aa7f34.
[24] J. Kang, H. Kim, K.S. Kim, S.-K. Lee, S. Bae, J.-H. Ahn, Y.-J. Kim, J.-B. Choi, B.H. Hong, High-performance graphene-based transparent flexible heaters, Nano Lett. 11 (2011) 5154–5158 https://doi.org/10.1021/nl202311v.
[25] J.J. Bae, S.C. Lim, G.H. Han, Y.W. Jo, D.L. Doung, E.S. Kim, S.J. Chae, T.Q. Huy, N. Van Luan, Y.H. Lee, Heat dissipation of transparent graphene defoggers, Adv. Funct. Mater. 22 (2012) 4819–4826 https://doi.org/10.1002/adfm.201201155.
[26] S.-Y. Lin, T.-Y. Zhang, Q. Lu, D.-Y. Wang, Y. Yang, X.-M. Wu, T.-L. Ren, High-performance graphene-based flexible heater for wearable applications, RSC Adv. 7 (2017) 27001–27006 https://doi.org/10.1039/c7ra03181e.
[27] T.H. Park, S. Yu, M. Koo, H. Kim, E.H. Kim, J.E. Park, B. Ok, B. Kim, S.H. Noh, C. Park, E. Kim, C.M. Koo, C. Park, Shape-adaptable 2D titanium carbide (MXene) heater, ACS Nano 13 (2019) 6835–6844 https://doi.org/10.1021/acsnano.9b01602.
[28] Y. Gong, J. Lin, X. Wang, G. Shi, S. Lei, Z. Lin, X. Zou, G. Ye, R. Vajtai, B.I. Yakobson, H. Terrones, M. Terrones, Beng K. Tay, J. Lou, S.T. Pantelides, Z. Liu, W. Zhou, P.M. Ajayan, Vertical and In-Plane heterostructures from WS_2/MoS_2 monolayers, Nat. Mater. 13 (2014) 1135–1142 https://doi.org/10.1038/nmat4091.
[29] Y. Gong, Z. Lin, G. Ye, G. Shi, S. Feng, Y. Lei, A.L. Elías, N. Perea-Lopez, R. Vajtai, H. Terrones, Z. Liu, M. Terrones, P.M. Ajayan, Tellurium-assisted low-temperature synthesis of MoS_2 and WS_2 monolayers, ACS Nano 9 (2015) 11658–11666 https://doi.org/10.1021/acsnano.5b05594.
[30] H. Ma, P. Chen, B. Li, J. Li, R. Ai, Z. Zhang, G. Sun, K. Yao, Z. Lin, B. Zhao, R. Wu, X. Tang, X. Duan, X. Duan, Thickness-tunable synthesis of ultrathin type-II dirac semimetal $PtTe_2$ single crystals and their thickness-dependent electronic properties, Nano Lett. 18 (2018) 3523–3529 https://doi.org/10.1021/acs.nanolett.8b00583.
[31] D. Jung, D. Kim, K.H. Lee, L.J. Overzet, G.S. Lee, Transparent film heaters using multi-walled carbon nanotube sheets, Sens. Actuators, A 199 (2013) 176–180 https://doi.org/10.1016/j.sna.2013.05.024.
[32] D. Gies, Human Body impedance model at radio frequencies, 2016 IEEE Symposium on Product Compliance Engineering (ISPCE), (2016) 1-6. https://doi.org/10.1109/ISPCE.2016.7492845.
[33] K.-Y. Shin, J.-Y. Hong, S. Lee, J. Jang, High electrothermal performance of expanded graphite nanoplatelet-based patch heater, J. Mater. Chem. 22 (2012) 23404–23410 https://doi.org/10.1039/C2JM34196D.
[34] T.-Y. Zhang, H.-M. Zhao, D.-Y. Wang, Q. Wang, Y. Pang, N.-Q. Deng, H.-W. Cao, Y. Yang, T.-L. Ren, A super flexible and custom-shaped graphene heater, Nanoscale 9 (2017) 14357–14363 https://doi.org/10.1039/C7NR02219K.
[35] Y. Han, W.F. Lu, Structural design of wearable electronics suitable for highly-stretched joint areas, Smart Mater. Struct. 27 (2018) 105042 https://doi.org/10.1088/1361-665x/aadf05.
[36] H. Gleskova, S. Wagner, Z. Suo, A-Si:H thin film transistors after very high strain, J. Non-Cryst. Solids 266-269 (2000) 1320–1324 https://doi.org/10.1016/S0022-3093(99)00944-8.
[37] A. Ní Annaidh, K. Bruyère, M. Destrade, M.D. Gilchrist, M. Otténio, Characterization of the anisotropic mechanical properties of excised human skin, J. Mech. Behav. Biomed. Mater. 5 (2012) 139–148 https://doi.org/10.1016/j.jmbbm.2011.08.016.
[38] Y. Wang, Z. Yu, G. Mao, Y. Liu, G. Liu, J. Shang, S. Qu, Q. Chen, R.-W. Li, Printable liquid-metal@PDMS stretchable heater with high stretchability and dynamic stability for wearable thermotherapy, Adv. Mater. Technol. 4 (2019) 1800435 https://doi.org/10.1002/admt.201800435.
[39] A.M. Hussain, E.B. Lizardo, G.A. Torres Sevilla, J.M. Nassar, M.M. Hussain, Ultrastretchable and flexible copper interconnect-based smart patch for adaptive thermotherapy, Adv. Healthcare Mater. 4 (2015) 665–673 https://doi.org/10.1002/adhm.201400647.
[40] N.S. Jang, K.H. Kim, S.H. Ha, S.H. Jung, H.M. Lee, J.M. Kim, Simple approach to high-performance stretchable heaters based on kirigami patterning of conductive paper for wearable thermotherapy applications, ACS Appl. Mater. Interfaces 9 (2017) 19612–19621 https://doi.org/10.1021/acsami.7b03474.
[41] P. Won, J.J. Park, T. Lee, I. Ha, S. Han, M. Choi, J. Lee, S. Hong, K.-J. Cho, S.H. Ko, Stretchable and transparent Kirigami conductor of nanowire percolation network for electronic skin applications, Nano Lett. 19 (2019) 6087–6096 https://doi.org/10.1021/acs.nanolett.9b02014.
[42] P. Zeng, B. Tian, Q. Tian, W. Yao, M. Li, H. Wang, Y. Feng, L. Liu, W. Wu, Screen-printed, low-cost, and patterned flexible heater based on Ag fractal dendrites for human wearable application, Adv. Mater. Technol. 4 (2019) 1800453 https://doi.org/10.1002/admt.201800453.
[43] T. Dinh, H.-P. Phan, A. Qamar, N.-T. Nguyen, D.V. Dao, Flexible and multifunctional electronics fabricated by a solvent-free and user-friendly method, RSC Adv. 6 (2016) 77267–77274 https://doi.org/10.1039/C6RA14646E.